

## Article

# Regional Responses of the Northern Hemisphere Subtropical Jet Stream to Reduced Arctic Sea Ice Extent

José Luis Rodríguez Solís <sup>\*,†</sup>, Cuauhtémoc Turrent <sup>†</sup> and Markus Gross <sup>†,‡</sup>

Department of Physical Oceanography, Ensenada Center for Scientific Research and Higher Education, CICESE, Ensenada 22860, Mexico; turrentc@cicese.mx (C.T.); mgross@cicese.mx (M.G.)

\* Correspondence: jrodriguez@cicese.edu.mx

† These authors contributed equally to this work.

‡ Deceased 25 January 2022.

**Abstract:** The effect of Arctic sea ice loss on the boreal winter regional trends of wind speed and latitudinal position of the Northern Hemisphere subtropical jet stream (STJ) in 1980–2012 is investigated. Two sets of global simulations with reduced Arctic sea ice extent are analyzed: simulations that, south of 70 N, use a climatological annual cycle of the sea surface temperature (SST) and a second set that uses full SST variability. Results with the climatological SST have a significant but weak response of the STJ wind speed and latitudinal position to the warmer Arctic: the wind speed generally decreases and the jet core is displaced equatorward. However, in the realistic SST simulations, the effect of Arctic warming is only slightly evident in a small equatorward shift of the jet over the Atlantic basin. Over the Pacific basin the STJ is mostly driven by tropical and mid-latitude SST variability, with little influence from the Arctic region. A weakening and poleward shift of the STJ that is observed in the realistic SST simulations over the Pacific basin is attributed to negative SST trends in the tropical Pacific and the consequent weakening of the mid-latitude meridional gradient of geopotential height in the upper troposphere.

**Keywords:** subtropical jet stream; arctic warming; global circulation model; climate variability



**Citation:** Rodríguez Solís, J.L.; Turrent, C.; Gross, M. Regional Responses of the Northern Hemisphere Subtropical Jet Stream to Reduced Arctic Sea Ice Extent. *Climate* **2022**, *10*, 108. <https://doi.org/10.3390/cli10070108>

Academic Editor: Salvatore Magazù

Received: 15 June 2022

Accepted: 10 July 2022

Published: 16 July 2022

**Publisher's Note:** MDPI stays neutral with regard to jurisdictional claims in published maps and institutional affiliations.



**Copyright:** © 2022 by the authors. Licensee MDPI, Basel, Switzerland. This article is an open access article distributed under the terms and conditions of the Creative Commons Attribution (CC BY) license (<https://creativecommons.org/licenses/by/4.0/>).

## 1. Introduction

The temperature contrast between the tropics and polar regions is the cause of subtropical jet streams (STJ) [1,2]. In the Northern Hemisphere, the recent rapid Arctic warming [3–6] has weakened the mid-latitude meridional temperature gradient in the lower atmosphere [5,7]. Furthermore, recent studies have found that the warming of the subtropical oceans observed since 1979 has induced an expansion of the Hadley Cells (HC) [8,9]. These two competing elements have led to a “tug of war” for the latitudinal position and strength of the STJ [10–13]. Observational studies indicate that in recent decades the STJ has shifted poleward [14–17] and is weaker [18]. These trends have been attributed to the widening of the tropics through the poleward shift of the latitude at which the meridional temperature gradients are largest [8,9]. Furthermore, the STJ responses to climate forcings have been found to differ regionally due to specific large-scale teleconnections patterns [14,16,17,19].

The rapid warming of the high latitudes has been proposed to cause an increase of geopotential heights in the polar troposphere, reducing both meridional thickness and surface temperature gradients, which in turn favor a weakening of the mid-latitude upper-level zonal wind field through the thermal wind relationship and ultimately cause the STJ to be wavier and slower [5,7,20]. In contrast to observational studies, numerical experiments with global climate models in which Arctic near-surface air temperatures are caused to increase through reduction of the sea ice extent have produced an equatorward displacement of the jet stream [21–28] and the sensitivity of its response to Arctic warming has also been found to differ regionally [29,30]. The link between the STJ and the Arctic is

not well established and continues to be the subject of scientific research due to the low statistical significance found in the corresponding observations [11,31–33].

Like all other components of the atmospheric circulation, the STJ are subject to natural variability and are involved in different teleconnection patterns that depend on the jet's position and strength [34]. For example, on the Pacific basin interannual time scale, the El Niño Southern Oscillation (ENSO) modulates upper ocean heat content in the tropics, and is associated with the contraction (El Niño) and expansion (La Niña) of the HC, which in turn displaces the STJ from its climatological position towards the equator or polewards, e.g., [8,35–37]. Similarly to ENSO, the Pacific Decadal Oscillation (PDO) has a strong influence on the size of the HC [38,39]. During boreal winter, the speed -and to some extent the latitudinal position- of the North Atlantic STJ is affected by the North Atlantic Oscillation (NAO) [40,41]. At high latitudes, the dominant mode of variability of the sea level pressure (SPL) is the Arctic Oscillation (AO) [42], which has regionally differing effects on the STJ and mid-latitude eddy activity [43]. For example, when the AO is in its positive phase, the STJ strengthens over Northwest Europe, but weakens over the Pacific basin [44]. Over East Asia and the Pacific Ocean, a major low-frequency variability mode is the Pacific North America pattern (PNA). Its positive phase is associated with an increase in the strength of the STJ over Asia which extends over the western Pacific, while its negative phase is related to a westward contraction over Asia [45].

In this work, we examine the variability of the intensity and latitudinal position of the boreal winter STJ over different regions of the Northern Hemisphere through the use of numerical experiments. The effect of Arctic warming (AW) induced by the loss of sea ice on the variability of the STJ is studied using a global climate model forced by two ocean states. The first uses a climatological sea surface temperature (SST) annual cycle to establish the STJ response to Arctic forcing, while a second set of experiments use complete SST variability to examine STJ trends in the context of natural climate variability. The 200 hPa geopotential height field and mid-latitude eddy activity are used to evaluate the influence of Arctic warming on the latitudinal position and intensity of the STJ over a 33 year period.

## 2. Methods and Data

The numerical model and experimental designs used in this work to simulate a warmer Arctic through reduction of its sea ice extent are described below. Indices and geographic regions used to analyze the STJ variability are also detailed.

### 2.1. Model Description

The atmospheric model used in this study is the Community Earth System Model (CESM) version 1.2.2 [46]. The full CESM model consists of coupled components for the atmosphere, ocean, land, and sea-ice. However, only the standard CESM component set F\_AMIP\_CAM5 was used, which runs the Community Atmosphere Model version 5 (CAM5) [47] in stand-alone mode, coupled to the Community Land Model version 4 [48]. The selected component set follows the Atmospheric Model Intercomparison Project (AMIP) protocol [49]. The simulations have a horizontal resolution of 2.5° longitude and 1.9° latitude with 30 vertical levels, extending to 3.6 hPa in a hybrid sigma-pressure vertical coordinate. Prescribed sea ice cover and SST data used for the surface boundary conditions are based on the reanalysis product from the Met Office Hadley Center Sea Ice and Sea Surface Temperature data set (HadISST) [50]. Data for the initial condition fields were obtained from the National Center for Atmospheric Research at <https://svn-ccsm-inputdata.cgd.ucar.edu/trunk/inputdata> (accessed on June 2022) and greenhouse gas concentrations, aerosols, solar variability, etc., are based on observational estimates [46,51]. The numerical simulations, described in the following section, were run to produce fifteen member ensembles for each control and experimental condition. Each model run has 34 years of integration, starting on the 1st of January 1979, with the first year discarded as spin-up. Therefore, each ensemble is made of a total of 495 simulated years. The individual members of any given ensemble differ from each other by random perturbations

(magnitude of  $1 \times 10^{-14}$ ) to the initial conditions of the atmospheric 3D temperature field [52], which, combined with the ensemble's size, ensure a reasonable spread over the possible pathways of the climate system in the model [53].

## 2.2. Experimental Design

We calculated two SST scenarios, each with control and reduced Arctic sea ice extent (low\_ice) experimental ensembles. The scenarios consist of:

1. simulations with a climatological SST annual cycle and,
2. simulations using full global SST variability.

The difference between the control and experimental simulations, in both experimental settings, was the treatment of the SST and sea ice extent fields in the Arctic region. For the low\_ice experiments, the annual cycles of the sea ice and SST fields at latitudes greater than  $70^\circ$  N were fixed to the 2012 annual cycle for all the simulated years. Observed data for this year marked a record (up to that year) for the lowest Arctic sea ice extent in recent decades as reported by the National Snow and Ice Center, NSIDC. In the  $60^\circ$  N to  $70^\circ$  N latitude band, the sea ice and SST data were linearly interpolated between the respective 2012 values and their corresponding lower latitude values, as necessary to avoid abrupt discontinuities in the SST fields. The description of the two experiments is given below.

Global climatological lower boundary condition experiments: We calculated control and experimental ensembles using a climatological (1979–2012) SST annual cycle below  $60^\circ$  N (referred to as *SST<sub>clim</sub>*). This configuration eliminates SST variability and its leading modes, such as ENSO, as the major source of internal climate variability (ICV, e.g., [54–56]). In the control simulations, Arctic SST and sea ice conditions above  $70^\circ$  N were updated monthly with corresponding real values of each year. This maintained the long-term contribution of the Arctic warming to the polar lower boundary conditions in the control simulations. For the low\_ice experiments, the SST and sea ice annual cycles for the year 2012 were repeated annually poleward of  $70^\circ$  N.

Global variable lower boundary condition experiments: In these simulations (referred to as *SST<sub>real</sub>*), the control simulations use real SST and sea-ice conditions, updated monthly for the global domain. They therefore have the influence of tropical and midlatitude SST variability. As before, the low\_ice experiments repeat the 2012 Arctic surface boundary conditions northward of  $70^\circ$  N for every simulated year.

## 2.3. Regionalization and STJ Indices

Jet streams are not continuous across the globe over fixed latitude bands. In order to distinguish regional STJ variability, six sectors were defined *a priori* throughout the mid-latitudes of the Northern Hemisphere based on the calculations of wind speed and wind speed trends shown in Figure 1. The first two sectors cover the continental regions of Europe (Eu) and Asia (As) (Figure 1). The Pacific Ocean was divided into two parts: the Western Pacific (wP), which spans the section of the STJ with the highest wind speeds (Figure 1a), and the Eastern Pacific (eP), where the jet is weaker and more variable. These two regions are characterized by having very clear trends in the intensity of the STJ [18] (Figure 1b). Another continental region was defined over North America and the sixth one over the North Atlantic. STJ intensity and position indices were calculated for each of the regions, in addition to indices that describe the variability of the meridional geopotential gradients and mid-latitude grid-resolved eddy activity. The descriptive indices of the STJ are addressed below.

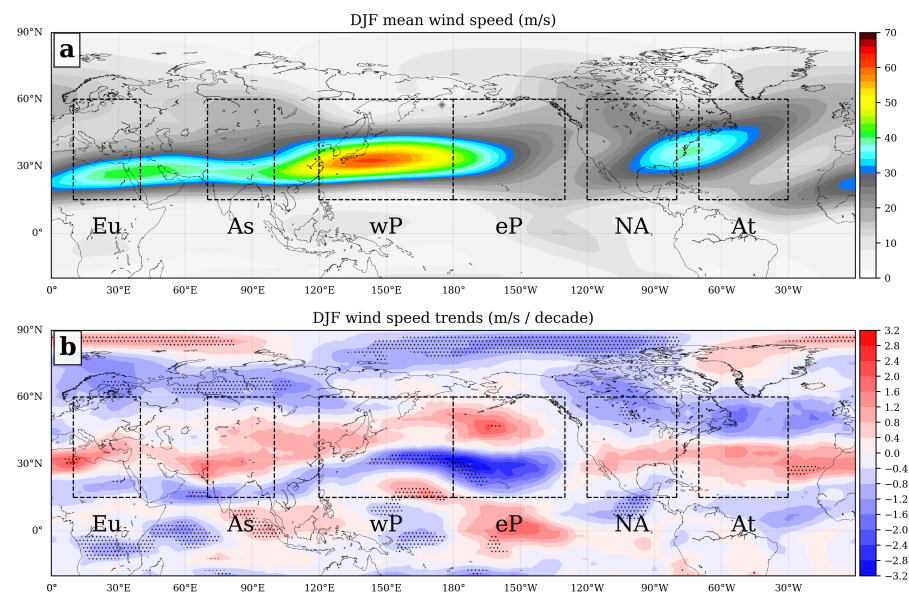


**Figure 1.** Winter (DJF) wind speed and wind speed trends between 400 and 100 hPa for the period from 1981 to 2012 following the methodology of Archer and Caldeira [18] with data from the National Centers for Environmental Prediction (NCEP) Reanalysis [57]. (a) Wind speed. (b) Wind speed trends. Domains regions for the calculation of descriptive STJ indices are enclosed in black boxes and labeled with their name abbreviations. Eu: Europe (10–40°W), As: Asia (70–100°W), wP: Western Pacific (120–180°E), eP: Eastern Pacific (180–130°E), NA: North America (120–80°E) and At: Atlantic (70–30°E). Dotted areas show statistical significant trends with 95% confidence level.

The latitudinal position and wind speed of the Northern Hemisphere STJ were calculated using mass flux-weighted averages between 400 hPa and 100 hPa and 15°N–60°N, following the metrics proposed by Archer and Caldeira [18]. The approach used to estimate the latitudinal position and intensity of the STJ is to weigh values by the mass transport. The idea of Archer and Caldeira [18] is that jet streams are regions characterized by high wind speed and mass transport. Therefore, the contribution of regions with low wind speeds to the value of the indices is minimized. Both the upper limit of atmospheric layer (100 hPa) and latitudinal band (15°N–60°N) used in the calculations were selected to focus the values of the indices on the STJ, avoiding the influence of the high latitude polar jet. An area-weighted average for each individual region of Figure 1 was also applied.

The 200 hPa geopotential height field was used to analyze changes in the meridional gradients using spherical coordinates. The term  $-r^{-1}\partial\phi/\partial\theta$  was area-weighted for each region in Figure 1 as follows:

$$GI = -\frac{\sum_{j=1}^m \sum_{i=1}^n \frac{1}{r} \frac{\partial\phi_{i,j}}{\partial\theta} a_{i,j}}{A}. \quad (1)$$

Here,  $\phi$  is the geopotential height at 200 hPa,  $a_{i,j}$  is a corresponding grid area,  $A$  indicates the total area of a given region,  $r$  is the radius of Earth,  $i$  and  $j$  indicate the latitude and longitude position of the grid points,  $\theta$  is the latitude, and  $n$  and  $m$  are the longitude and latitude grid sizes. This expression is normalized with the standard deviation ( $S$ ) to obtain a Normalized Gradient Index (NGI):

$$NGI = -\frac{GI - \mu_{ctl}}{S_{ctl}}, \quad (2)$$

where  $\mu_{ctl}$  is the temporal average and  $S_{ctl}$  is the standard deviation of  $GI$ , both for the control ensemble. The index has values between  $-3$  and  $3$ . Positive (negative) values imply strong (weak) meridional gradients of the geopotential field.

Mid-latitude eddy activity was quantified using the eddy momentum flux convergence, as proposed by Li and Wettstein [58]:

$$E = \frac{1}{r \cos^2 \theta} \frac{\partial(u'v' \cos^2 \theta)}{\partial \theta}, \quad (3)$$

where primed values were obtained with a 10th order Butterworth bandpass filter [59] with a 2–8 day cutoff period, which is appropriate for the mid-latitude synoptic timescales such as those of extratropical cyclones or Rossby waves [60–63]. Using spherical coordinates, the index ( $iE$ ) is also defined as a mass- and area-weighted average:

$$iE = \frac{\sum_{k=p1}^{p2} \sum_{j=1}^m \sum_{i=1}^n E_{i,j,k} \Delta p_{i,j,k} a_{i,j,k}}{P \cdot A}. \quad (4)$$

Here,  $\Delta p_{i,j,k}$  is the pressure difference between levels  $k$  and  $k - 1$ , and  $P = p1 - p2$ . The values for  $p1$  and  $p2$  are 400 hPa and 100 hPa, respectively. As in *NGI*, the  $iE$  index was normalized with the standard deviation. All indices were time-averaged over the winter season, December to February (DJF).

#### 2.4. Other Statistics and Climatic Indices

Additionally, the two-tailed Student's  $t$ -test was performed to determine the statistical significance of the differences between the control and experimental ensembles. All trends were calculated using the 'Sen' slope estimate method [64], using the non-parametric Mann-Kendall test for statistical significance [65].

Different winter climatic indices were used to explore their relationship with the intensity and latitudinal position of the STJ in the control and experimental ensembles. Indices for the AO, NAO, and PNA were calculated from the definitions compiled by the Climate Prediction Center (available online at [https://www.cpc.ncep.noaa.gov/products/precip/CWlink/daily\\_ao\\_index/teleconnections.shtml](https://www.cpc.ncep.noaa.gov/products/precip/CWlink/daily_ao_index/teleconnections.shtml) (accessed on June 2022) and references therein) with data from the control and experimental ensembles of the *SSTreal* case.

The AO index is computed from the normalized series of the leading mode of the Empirical Orthogonal Function (EOF) analysis of geopotential height anomalies at 700 hPa in the 20 N–90 N domain. Likewise, the NAO index is calculated from the first EOF mode of the 500 hPa standardized geopotential height anomalies in the 20 N–80 N and 90 W–40 E domain. The index for the PNA was calculated using the modified Pointwise method used in Wallace and Gutzler [66] with standardized 500 hPa geopotential height anomaly data. The anomalies used in the computation of the climatic indices are referenced to the period 1981–2000.

The Oceanic Niño Index (ONI) was used to represent the Pacific Ocean tropical variability. ONI data were obtained from <https://www.cpc.ncep.noaa.gov> (accessed on June 2022). The Pacific Decadal Oscillation (PDO) index was obtained from <https://www.ncdc.noaa.gov> (accessed on June 2022), calculated using the HadISST1.1 dataset.

For the NAO and PNA composites, only winters with a strong index value ( $|\text{index}| > 0.5$ ) were selected. Positive phase ENSO winter composites were calculated for the winters: 80, 83, 87, 88, 92, 95, 98, 03, 05, 07, 10 and 11, and negative ENSO: 84, 85, 89, 96, 99, 00, 01, 06, 08, 09, 12. Winters were selected with the DJF mean ONI index and are referred to here by the year of the month of February of each selected season.

### 3. Results

The results are organized as follows. First, in Section 3.1, we examine the large scale winter atmospheric response to the imposed changes in the sea ice and SST fields over the Arctic region through the responses of the near-surface air temperature (T2m) and sea level

pressure (SLP), and upper troposphere (200 hPa) geopotential height. Zonal winds are analyzed in Section 3.2. Statistics for the position and wind speed of the STJ are presented in Section 3.3. Regional time series of the STJ indices are analyzed in Section 3.4. Finally, in Section 3.5 we explore changes in the relation between the STJ and the different climate oscillations under Arctic warming conditions, using the *SSTreal* simulations.

### 3.1. Large Scale Climate Response in the Arctic Warming Experiments

Both experimental ensembles with low sea ice extent in the Arctic produced warmer conditions in the high latitude lower atmosphere (Figure 2a,c). The near-surface temperature responses in both cases have similar spatial patterns. The strongest warming occurred over the Barents and Kara Seas, with winter mean temperature differences greater than 10 °C between the control and experimental ensembles. The experimental conditions produced warming greater than 5 °C over the Canadian Archipelago. Negative anomalies, of up to −3 °C, occurred in the Aleutian and Icelandic Low regions. Weaker anomalies of −0.5 °C occurred over Asia and Eastern Europe, but they were only statistically significant in the *SSTclim* case. Even though the negative anomalies over Eurasia are small, this feature is similar to the “Warm Arctic—Cold Continents” (WACC) pattern that has been recognized as an effect of the reduction of Arctic sea ice [5,67–70]. Some studies have suggested that this pattern results from warmer Arctic conditions favoring the occurrence of negative NAO/AO events, which in turn are associated with more severe winters over Eurasia [5,28,67,68,71,72]. The WACC pattern has also been identified in General Circulation Models (GCMs) that used low prescribed Arctic sea ice extent., e.g., [28,68,73].

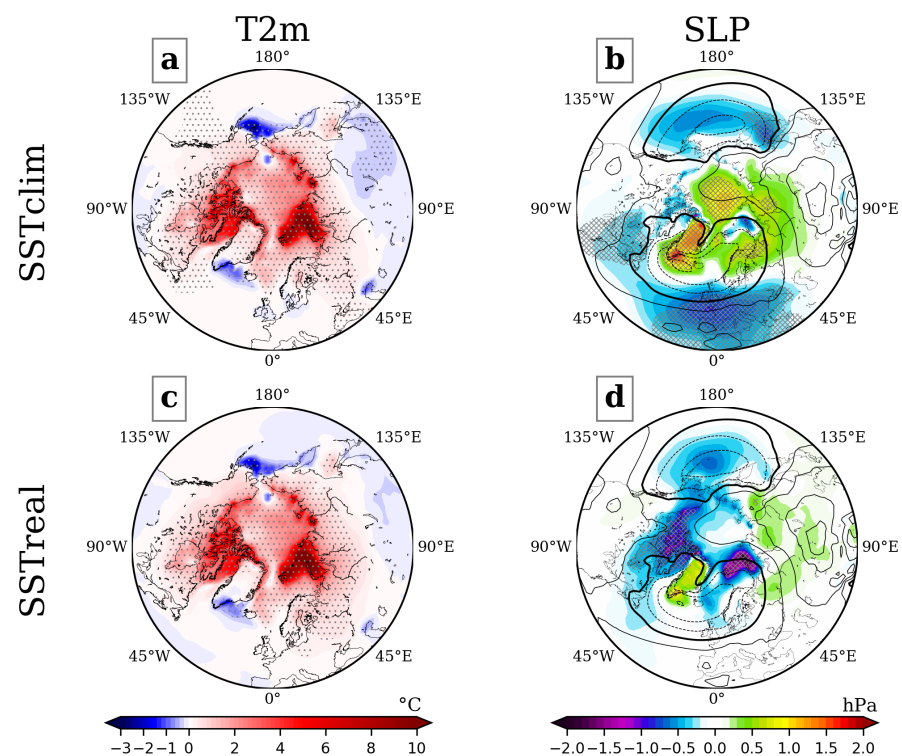


**Figure 2.** Winter ensemble-mean responses (experiment minus control) in the lower atmosphere. Two-meter air temperature (T2m) (a,c); sea-level pressure (SLP) (b,d). Results are given for the *SSTclim* and *SSTreal* cases. The black contours in the SLP plots show the corresponding climatological values from the control ensemble (the bold line is the 1015 hPa isobar; values greater/less than 1015 hPa are shown with continuous/dashed lines and the contour interval is 5 hPa). Dotted (T2m) and hatched (SLP) areas indicate regions where the differences are statistically significant at the 95% confidence level.

In the *SSTclim* case, the SLP response has positive anomalies over most of the Arctic Ocean (Figure 2b). Positive responses greater than 1 hPa were observed from the East Siberian Sea to the Kara Sea, as has been described in previous studies [28,68,74–76]. These anomalies are related to the strengthening and northward elongation of the Siberian high pressure system, which in turn is linked to the small negative temperature anomalies that occurred in that region. The slight northward shift of the Siberian high produced a southward displacement and weakening of the Icelandic Low and hence the positive anomalies over Greenland and negative anomalies over the North Atlantic. Small negative anomalies,  $-0.5$  hPa, were observed in the Aleutian Low region. Although in our results these anomalies are nonsignificant, they correspond to an intensification of that pressure system [12,74,76–78].

In the *SSTreal* case, negative anomalies also occurred in the Aleutian Low region. This SLP response has been consistently reported by numerical studies that used low prescribed Arctic sea ice extent and climatological SST [76], similar to our *SSTclim* case. It is noteworthy to observe that the intensification of the Aleutian low as a response to Arctic sea ice loss persisted even when full SST variability is used (Figure 2d). The positive SLP response over Siberia in *SSTreal* has a smaller magnitude compared to the *SSTclim* case and is not significant. Because the Siberian High did not extend northward in *SSTreal* as it did in *SSTclim*, the SLP response over the Arctic was more influenced by the near-surface warming produced by sea ice loss in the former than in the latter case. This explains the differences observed between both SLP responses, despite the fact that the T2m responses are similar.

The response of the upper troposphere to the experimental conditions was examined with the winter 200 hPa geopotential height field (Z200). In Figure 3a, positive anomalies are observed over the Arctic, extending to 60°N and even lower latitudes over Eurasia and the North Atlantic. The largest differences are observed in the *SSTclim* case, with anomalies greater than 20 m coinciding with locations where the T2m anomalies are also strongest. The magnitude of the response over the Arctic decreased in the *SSTreal* case (Figure 3b) because of the greater interaction between high and lower latitudes driven by the SST variability and the corresponding increased variance of Z200.

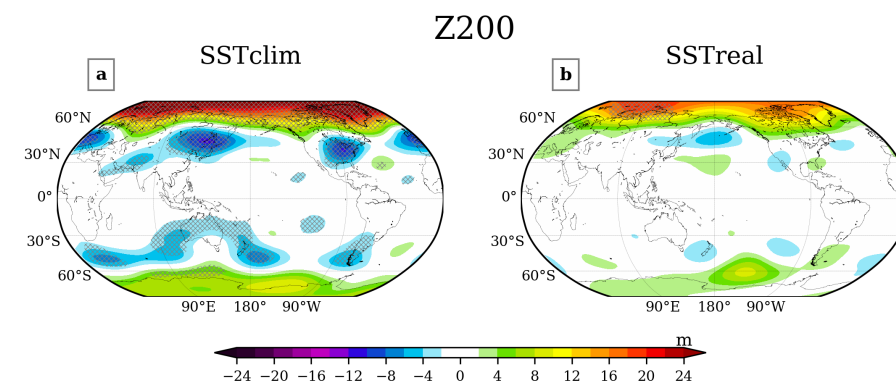


**Figure 3.** As in Figure 2, but for the winter 200 hPa geopotential height field. (a) For *SSTclim* case and (b) For *SSTreal* case.

The Z200 response in the mid-latitudes was markedly different in the two experimental cases. Strong mid-latitude negative Z200 anomalies were observed in the *SSTclim* case over eastern Asia, eastern North America and western Europe. Previous studies have found a similar atmospheric response to reduced Arctic sea ice that resembles the negative AO phase, with tropospheric expansion and a weakened polar vortex [30,67,79–81]. The mid-latitude negative anomalies seen in Figure 3a are related to blocking patterns over those regions that have also been addressed in previous literature [82–85].

In the *SSTreal* case (Figure 3b), the mid-latitude negative anomalies are only observed over the southern Bering Sea and they are weak and non-significant. In addition, the

negative anomalies observed over Europe in *SSTclim* shifted to a weak positive response in *SSTreal*.

The clear differences in the low-sea ice experimental responses between the idealized *SSTclim* case and the realistic *SSTreal* case illustrate that the mid-latitude response to Arctic warming is diminished by natural variability. The effects of the Arctic low-level atmospheric warming on the upper tropospheric expansion are meaningfully different when the full variability of the SST is used, as is illustrated by the results presented below.

### 3.2. Regional Response of the Zonal Wind

The mean zonal wind response for each region is shown in Figure 4. A robust characteristic of the zonal wind response to the reduction of Arctic sea ice in numerical models has been the weakening of the westerly winds north of 50N, in the poleward flank of the jet [28,76]. A similar response was found in this work. Both SST cases had weaker zonal winds in the high latitudes (approximately 50 N to 80 N) that extended from the surface to the upper troposphere and lower stratosphere. This weakening of the zonal wind was greatest in the upper atmosphere and is consistent with the Z200 pattern seen in Figure 3. It is therefore the response of the circulation to the thermal expansion of the troposphere over the Arctic region, as expected from the thermal wind relation. As with Z200, the magnitude of the response was also weaker in the *SSTreal* case.

In the mid-latitudes, the response pattern in Figure 4 has alternating signs, especially near the height of the STJ core (between 500 hPa and 100 hPa). Similar results have been reported in other studies, and the pattern is attributed to an equatorward shift of the STJ [28,74–76]. A detailed discussion of this point is given below. Again, the differences were smaller in magnitude in the *SSTreal* case.

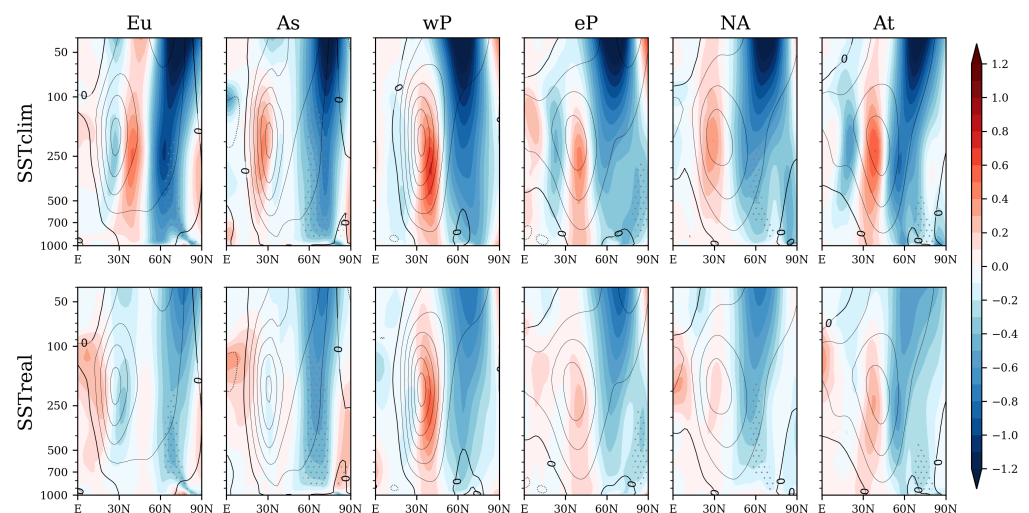


**Figure 4.** Regional winter responses of the zonal mean zonal wind ( $\bar{u}$ , m/s, where the overbar indicates a zonal average), plotted as a function of latitude and height (hPa) for the *SSTclim* (top) and *SSTreal* (bottom) cases. The black contours show the corresponding climatologies of the control ensembles (contour interval every 10 m/s with dashed lines for negative values). Dotted areas indicate regions where the differences between the experimental and control ensembles are statistically significant at the 95% confidence level.

### 3.3. STJ wind Speed and Position

The longitudinal responses of the wind speed and latitudinal position of the STJ that are shown in Figure 5 were calculated using the metrics described above (Section 2.3). This calculation was made to determine which regions had larger STJ responses to Arctic warming and how those responses compare to different measures of the internal climate variability. In the *SSTclim* case (red curve, Figure 5a) the winter STJ was significantly weaker compared to the control ensemble in the **Eu** region, with a mean difference in

intensity of  $-0.2$  m/s. Similar negative responses occurred in the **NA** and **At** sectors. In the *SSTreal* case the STJ was weakened in the experimental ensembles throughout most of the Northern Hemisphere except in the **eP** region, but the response was not significant. A positive response of the STJ intensity occurred in the **As** region and in most of the Pacific basin in the *SSTclim* case, and in the **eP** region in *SSTreal*.

The STJ generally responded to the Arctic low-ice forcing with an equatorward displacement of the jet core (Figure 5e). This result agrees well with recent studies, e.g., [27,28,76]. The displacements were larger and statistically significant in the *SSTclim* case ( $>0.2$  degrees of latitude in the **Eu**, **NA** and **At** regions). Notably, the displacement did not occur in the central (in the case of *SSTclim*) or eastern (for *SSTreal*) Pacific regions.

Using well established methodologies (see Section 2.4), climate indices for the NAO, PNA and ENSO were calculated from the *SSTreal* simulations. A composite analysis of the STJ wind speed and latitudinal position was then computed for each climate oscillation (Figure 5b–h). The corresponding long term mean of the *SSTreal* control ensemble was subtracted from the average winter values of positive and negative years of the NAO, PNA and ENSO, for both the control and experimental results of *SSTreal*.

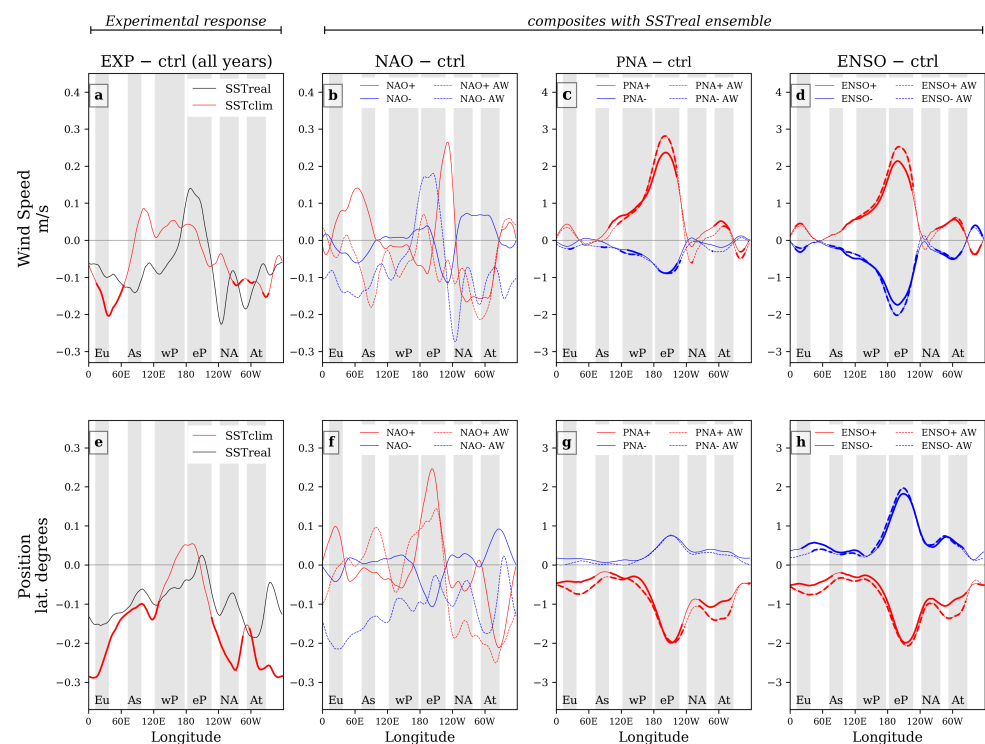


**Figure 5.** Experimental response and composite analysis for climatic oscillations of the winter STJ wind speed and latitudinal position, plotted as a function of longitude. (a) Wind speed differences between DJF ensemble means (experiment-control) for the *SSTclim* and *SSTreal* cases, (b) NAO composite analysis for wind speed from the *SSTreal* ensembles, (c) corresponding PNA analysis, and (d) corresponding ENSO analysis. The lower plots (e–h) are the same but for the STJ latitudinal position. Bold curves indicate regions where the differences are statistically significant at the 95% confidence level.

The positive NAO winter composite for the control ensemble (red continuous curve in Figure 5b) had a stronger STJ over Eurasia and the eastern Pacific compared to the long term mean. During negative phase events, the STJ was weaker over Eurasia and the eastern Pacific, and stronger in the **NA** and **At** regions, mirroring the behaviour of the positive NAO phase. Despite the fact that the effect of the NAO on the STJ wind speed and latitudinal position was not significant in either *SSTreal* ensemble, the positive and negative NAO composites from the control ensemble have a response that roughly mirrors each

other in every region. This result suggests that the NAO climatic pattern is well captured in the modeled atmosphere, as is its influences on the strength and position of the STJ. It is interesting to note that this mirrored relation is lost in the warmer Arctic ensemble. Compared to the results from the control ensemble, both positive and negative NAO events in the warmer Arctic ensemble produced a weaker STJ in all regions except in eP.

In the NAO analysis for the STJ latitudinal position (Figure 5f), the most notable difference with a warmer Arctic was the greater equatorward displacement of the jet stream during negative NAO events (again with the exception of the eP region). This result can be related to the occurrence of more blocking patterns over Greenland, as has been suggested by previous studies, e.g., [40,82,84,86] that have linked stronger negative NAO events to Arctic warming conditions [72,87,88].

Unlike the NAO composites, which have differences that are of similar magnitudes to those of both experimental responses to Arctic warming (compare Figure 5a vs. Figure 5b and Figure 5e vs. Figure 5f), the ENSO and PNA oscillations produced STJ wind speed and latitudinal position responses that are an order of magnitude greater. The positive ENSO and PNA composites had an increase in STJ wind speed greater than 2 m/s in the eP region in the *SSTreal* control ensemble (Figure 5c,d). Responses to the negative ENSO and PNA events largely mirror those of the positive phase events. The strength of the responses to positive phase events increased slightly in the Arctic warming ensemble (red continuous and dashed lines in Figures 5c,d), but the experimental conditions had no effect on the STJ position response to ENSO and the PNA (Figure 5g,h).

Some aspects of the distributions of the wind speed and latitudinal position of the STJ are presented in Figure 6. The wind speed distributions of the STJ (Figures 6a,b) are similar in the control and experimental ensembles of both SST cases. However, the greater variability of the STJ wind speed in the *SSTreal* ensembles is also evident, especially over oceanic regions. In particular, the interquartile range increased by a factor of roughly ten over the Pacific Ocean in the realistic SST ensembles. The *SSTreal* wind speed response to the Arctic forcing (Figure 5a) is therefore reduced to a greater degree by the STJ variability (compared to *SSTclim*), which is a likely explanation for why it was not significant. The clearest effect of the Arctic warming on the STJ is the equatorward displacement which is evident in Figure 6c. Again, the greater climate variability of the *SSTreal* ensembles diminished this response. However, it is interesting to note to what degree the latitudinal position of the STJ (Figure 6d) is controlled by tropical, rather than polar, processes, especially over the Pacific basin.

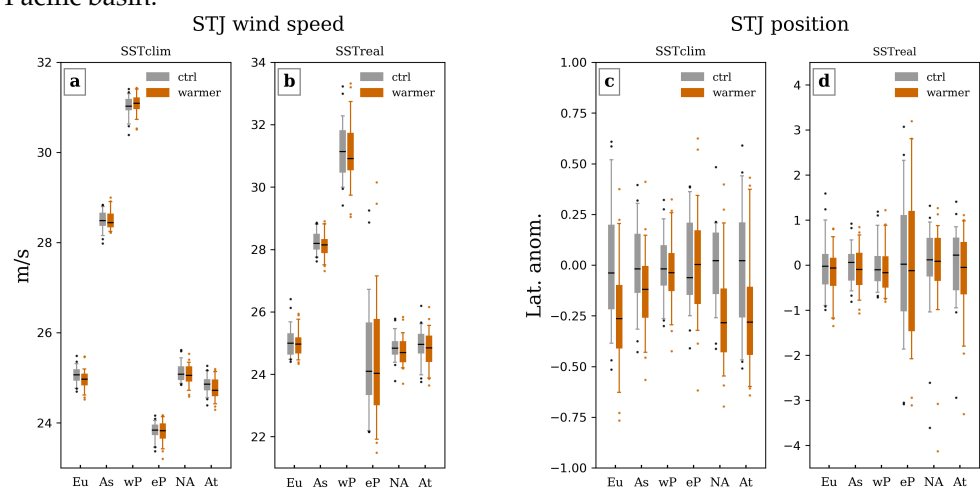


**Figure 6.** Box plots of the regional statistics of the STJ wind speed and latitudinal position. (a) Wind speed for *SSTclim*. (b) Wind speed for *SSTreal*. (c) Latitudinal position for *SSTclim*. (d) Latitudinal position for *SSTreal*. The central mark indicates the median and the bottom and top edges of the box indicate the 25th and 75th percentiles. The outliers are plotted individually using the “dot” symbol. Gray shading is used for the control ensembles and orange for the low-sea ice Arctic Warming ensembles. Note different scales of y axes.

### 3.4. STJ Indices

The following two subsections include results for the time evolution of the STJ wind speed, latitudinal position, *NGI* and *iE* indices, for both SST scenarios.

#### 3.4.1. *SSTclim* Case

Figures 7a,b show the variability of the STJ wind speed and latitudinal position for the *SSTclim* case. No significant trends over the study period that are attributable to the low sea-ice Arctic warming condition are observed. However, as mentioned above, an equatorward displacement of the STJ of  $\sim 0.25$  lat. degrees occurred in the **Eu**, **NA** and **At** regions (Figure 7b). The gradient index, shown in Figure 7c, indicates no significant changes over the study period in the mid-latitude meridional geopotential gradients, except in the **NA** and **At** regions, where a slight weakening of the gradients occurred. The *iE* index did not change under the warmer Arctic conditions, indicating that the mid-latitude eddy activity remained the same as in the control ensemble.

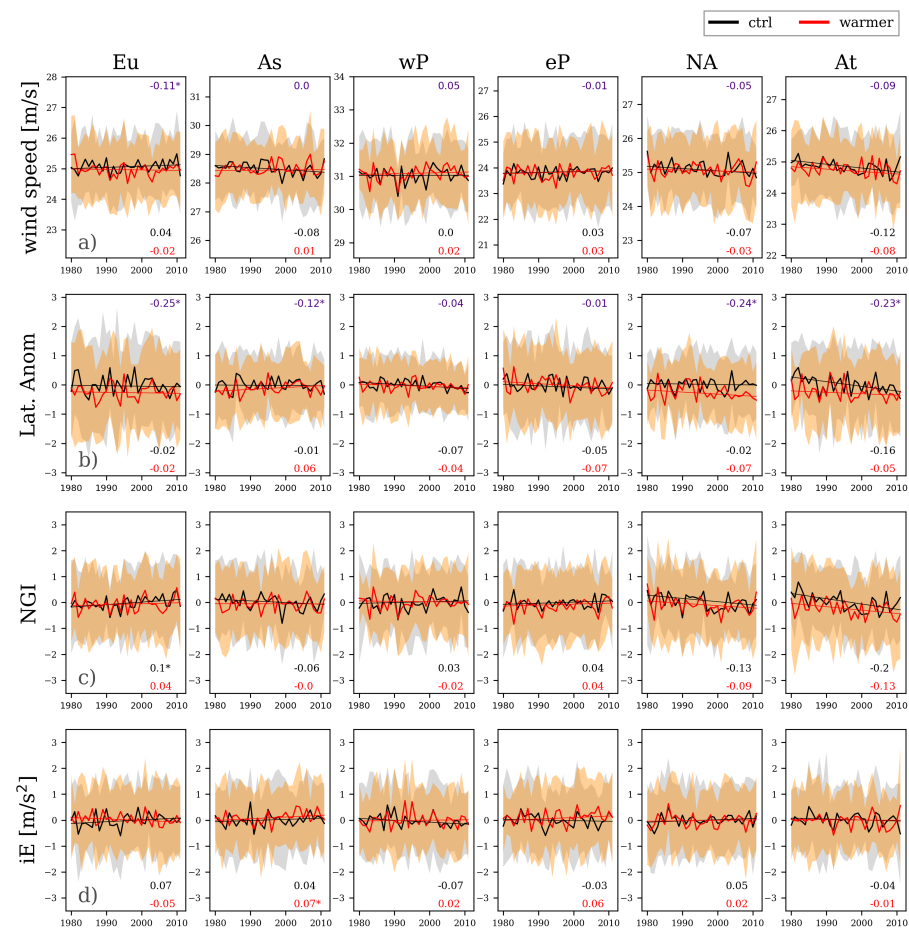


**Figure 7.** Time series of winter (DJF) mean indices of STJ variability for the *SSTclim* case. (a) STJ wind speed and (b) Latitudinal position, (c) *NGI* and (d) *iE* indices. Shaded areas indicate  $\pm 1.5$  times the standard deviation ( $\sigma$ ) across ensemble members: gray shading for the control ensemble and orange for the low-sea ice Arctic Warming ensemble. Solid curves plot the indices ensemble mean value and the straight lines are the corresponding linear regressions. Trends values (values per decade) estimated from the linear regression are indicated at the bottom right of each panel. The differences between the ensemble means are indicated in the upper right of each panel of the wind speed and latitudinal position plots. Values are marked with '\*' when the differences or trends are significant at the 95% confidence level. Note differences in scale in some *y* axes.

### 3.4.2. SSTreal Case

In this more realistic case, with full SST variability, no meaningful changes were observed between the control and experimental ensembles. The climatic variability induced by the SST diminished the southward positions of the STJ that are observed in *SSTclim*. However, the following observations can be made of the *SSTreal* results. There are strong negative trends of the STJ wind speed over the Pacific Ocean, mostly in the **eP** region (Figure 8a), both in the control and the experimental ensembles. Similar trends were found with observational data on the jet stream intensity [7,14,18]. Here, it is observed that when realistic SST variability is used, the Arctic sea-ice reduction does not influence the STJ wind speed (Figures 6b and 8a). However, another climatic factor that influenced both the experimental and control ensembles did weaken the STJ wind speed over the Pacific basin. It is addressed below.

As with the STJ wind speed, no significant changes occurred between the control and experimental ensembles for the latitudinal position (Figure 8b), with the exception of the **At** region, where the STJ was displaced southward by 0.19 lat. degrees in the experimental ensemble. This equatorward displacement was accompanied with a weakening of the meridional gradients (Figure 8c), and an increase of the mid-latitude eddy activity (Figure 8d). Furthermore, in the **eP** region, a significant positive trend was observed such that the jet stream shifted poleward in both *SSTreal* ensembles throughout the study period.

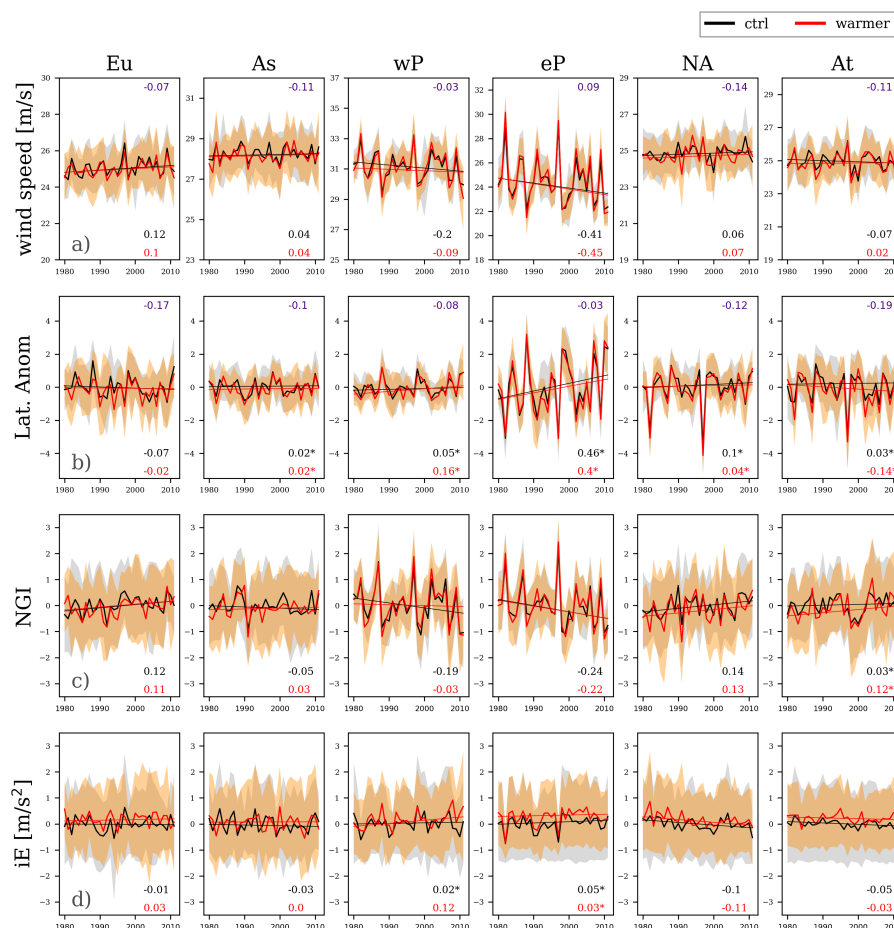


Figure 8. As in Figure 7, but for the *SSTreal* case.

The wind speed and latitudinal position variability of the jet stream over the Pacific basin are explained by the trends in the meridional geopotential gradients. Figure 8c presents the time series for the *NGI* index. When the *NGI* is positive (negative), the STJ wind speed increases (decreases) and is displaced equatorward (poleward). An intense

(and more zonal) jet allows less elongations and synoptic events at mid-latitudes. Hence the *iE* decreases (increases). This relation is stronger in the **eP** region ( $r(NGI, ENSO) = 0.91$ ) than in the **wP** ( $r(NGI, ENSO) = 0.81$ ) sector. It can be most clearly observed in years with strong El Niño events in Figure 8a,b (1983 and 1998). This result suggests that STJ variability over the Pacific basin is mostly thermally driven [58,89].

### 3.5. Correlations between the STJ and Ocean-Atmosphere Climate Oscillations

Correlations between the wind speed and latitudinal position ensemble mean series from *SSTreal* (showed in Figures 8a,b) and corresponding ocean-atmosphere oscillation indices (PDO, ENSO, PNA, NAO, and AO) were computed. The results show that ENSO, PNA and the PDO are the leading modulators of the winter variability of the STJ strength and latitudinal position. The STJ strengthens (weakens) when the tropical Pacific SST increases (decreases) (Figure 9a). A concurrent equatorward (poleward) displacement of the STJ is also observed (Figure 9b). Furthermore, it was also found that the relationship between the STJ and climatic oscillations may be affected by warming of the Arctic region, with changes strongly depending on the specific climatic oscillation and the STJ region (compare Figure 9a–c and Figure 9b–d).

The correlation between the STJ wind speed and the ENSO and PNA indices decreased strongly over the **NA** continental region in the *SSTreal* Arctic warming experiments (Figure 9c). The ENSO correlation with STJ wind speed also decreased to a non-significant value over the continental **As** region. However, this weakening of the ENSO and PNA correlations over continental regions did not occur with the latitudinal position of the STJ (Figure 9d). The corresponding analysis with the NAO index does not have significant correlations for either STJ variable. However, the results for the AO index showed an interesting doubling of the strength of the correlation with the latitudinal position of the STJ in the **NA** and **At** regions in the warmer Arctic ensemble.

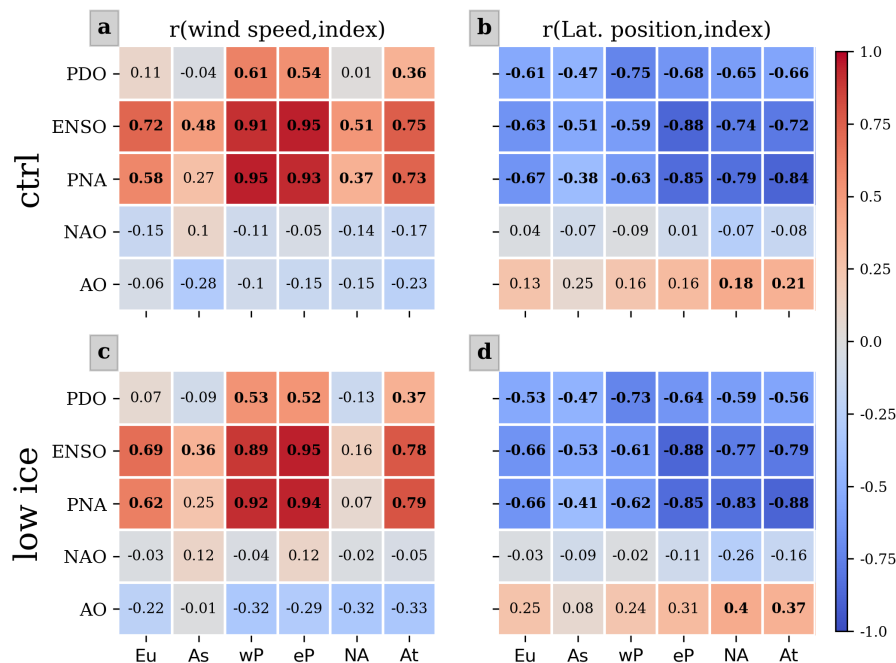


**Figure 9.** Pearson correlation between winter STJ wind speed and latitudinal position from the *SSTreal* case and ocean-atmosphere climate oscillation indices. (a) STJ wind speed from the control ensemble, (c) STJ wind speed from the experimental ensemble, (b) position from the control ensemble and (d) position from the experimental ensemble. Bold numbers indicate statistical significance at the 95% confidence level.

### 3.6. Discussion and Conclusions

The warmer Arctic conditions of the *SST<sub>clim</sub>* experimental ensemble resulted in weaker STJ wind speeds over the North American, Atlantic, and European regions. These regions were also more sensitive to equatorward shifts of the jet in response to Arctic sea ice loss. The southward shift of the STJ is related to the geopotential height response in the upper troposphere, and could be explained by an increase in the frequency of occurrence of blocking patterns in these regions. Furthermore, in the North American and Atlantic regions, the *NGI* index showed that the meridional gradients of geopotential height were weakened when the Arctic sea ice extent was reduced.

It is interesting to note that opposite trends have been observed in the Southern Hemisphere, where Antarctic cooling in the upper atmosphere, a product of the ozone hole, has led to a strengthening and poleward shift of the westerly winds [90,91].

In the *SST<sub>real</sub>* case, an equatorward shift in the latitudinal position of the STJ was also observed in the **At** region. Using observational data, Woollings et al. [40,86] suggest that the negative NAO regime favors a southern displacement of the jet position, with positive geopotential height anomalies over Greenland and negative ones over the Atlantic. Similar results were found in this work in the *SST<sub>real</sub>* simulations, although the negative geopotential height anomalies over the Atlantic were weak and not significant.

The correlations of the STJ latitudinal position with the AO roughly doubled in the **NA**, **At**, and **Eu** regions under the warmer Arctic conditions. It also increased for the NAO in the **eP**, **NA**, and **At** regions, though not to the statistically significant level. The increased relation in those regions between the position of the STJ and the AO in the warmer Arctic *SST<sub>real</sub>* ensemble is consistent with previous results based on observations and climate model outputs that have suggested that reduced sea ice over the Arctic tends to produce winter circulation patterns that resemble the negative phases of the NAO/AO [22,72,79,80,92]. Similar high latitude atmospheric responses were found in this work (Section 3.1). Negative AO events weaken the polar vortex [30,79–81], positioning the STJ equatorward.

The *SST<sub>real</sub>* ensemble showed that the STJ is weakening and shifting poleward over the Pacific basin, especially in the **eP** region. The model results suggest that these trends are not forced by Arctic sea ice loss because both the control and experimental ensembles have similar trends over the study period.

Figure 10a shows the SST trend for the period 1980–2012 estimated from the HadSS T1.1 [50] reanalysis data. Unlike most of the global ocean, a cooling trend that has been addressed in previous studies [93–97] is observed in the Central and Eastern tropical Pacific Ocean. It extends poleward along the Americas and is related to the phase change (from positive to negative) of the Pacific Decadal Oscillation that occurred during the study period [39,94,98,99]. The effects on the atmosphere of the negative Pacific SST trends are visible in the tropical upper troposphere, where the geopotential height trend is close to zero. Significant positive Z200 trends are observed over the North Pacific (Figure 10b) induced by positive SST trends. The net effect of the SST trend pattern in the mid-latitude North Pacific is a weakening of the meridional upper geopotential height gradients (as a direct response to the weakening of the meridional SST gradient), as shown in Figure 8c. Thus the jet stream is weakened and shifted poleward, and increased synoptic activity occurs in the mid-latitudes (Figure 8d) due to a wavier STJ [100,101]. In addition, the PDO phase change from positive to negative is related to a poleward expansion of the Hadley Cell [39,94], which drives the STJ in the same direction. This argument is supported by studies that have shown that the Northern Hemisphere Pacific STJ is mostly modulated by central Pacific SST variability [58,89,102–105].

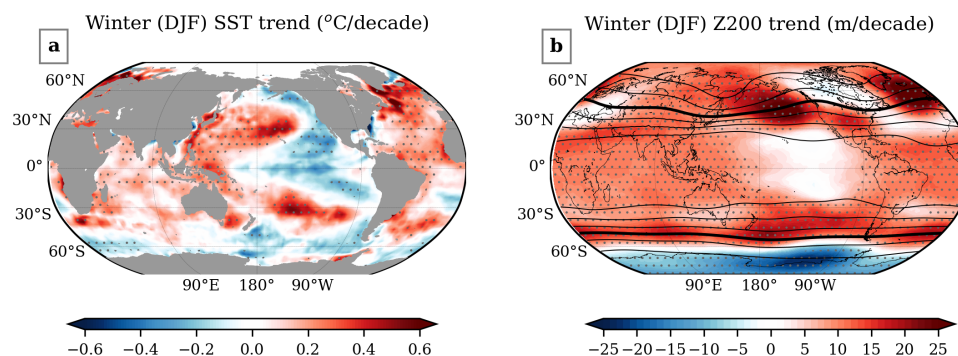


**Figure 10.** (a) SST trends (Data: HadISST1.1) and (b) geopotential height trend at 200 hPa (Data: *SST<sub>real</sub>* control ensemble mean). Trends were calculated for the 1980–2012 period. The black contours in (b) show the corresponding climatological values of Z200 from the control ensemble (the bold line is the  $1.15 \times 10^4$  m contour and the contour interval is 250 m). Dotted areas indicate statistical significance at the 95% confidence level.

In summary, numerical experiments in which Arctic warming is induced by the loss of sea-ice have a consistent but limited Arctic influence on the STJ latitudinal position over Europe, North America and the North Atlantic basin. A slight effect on the STJ wind speed is also observed in those regions, but is diminished below statistically significant levels when realistic internal climate variability is used in the numerical simulations. The experiments with full SST variability demonstrated that the weakening trend and poleward drift of the Pacific STJ that occurred over the period 1980–2012 and that are addressed by other studies [14,18] are not a consequence of Arctic sea ice loss but rather were forced by the Pacific Decadal Oscillation phase change. The variability of the STJ in the NA and At regions are closely related to the AO, and the results of the numerical simulations presented here suggest that they can have a greater influence on the STJ under warmer Arctic conditions.

As a final remark, we note that in this work thirty year trends of the wind speed and latitudinal position of the STJ are analyzed under warmer Arctic conditions using numerical simulations that are similar to those used in previous studies, e.g., [22,24,79,106]. However, here, we have also included a set of experiments in which the full observed variability of the SST over the period 1979–2012 was used. These types of realistic simulations have not been broadly used to analyze the sensitivity of climate teleconnections to the effects of Arctic sea ice loss, which our study only begins to address. Future work that analyzes the mechanisms involved in SST-driven STJ variability is needed, as are studies that focus on the individual climate oscillations (e.g., perpetual ENSO simulations with experimental conditions for the Arctic similar to those used here). In addition, results from climate models that use active ocean-atmosphere-sea ice coupling might differ from those presented here because of the importance of different feedback mechanisms.

**Author Contributions:** Conceptualization, J.L.R.S., C.T. and M.G.; Data curation, J.L.R.S.; Formal analysis, J.L.R.S.; Funding acquisition, C.T. and M.G.; Investigation, J.L.R.S., C.T. and M.G.; Methodology, J.L.R.S., C.T. and M.G.; Project administration, C.T. and M.G.; Resources, C.T. and M.G.; Supervision, C.T. and M.G.; Validation, J.L.R.S.; Visualization, J.L.R.S.; Writing—original draft, J.L.R.S.; Writing—review & editing, C.T. All authors have read and agreed to the published version of the manuscript.

**Funding:** This research was funded by the National Council of Science and Technology (CONACYT) grant no. 414615 and by the Laboratorio Nacional de Supercomputo del Sureste de Mexico (LNS) through project No. 201803026.

**Acknowledgments:** We thank CONACYT for the Ph.D. Scholarship Grant 414615 awarded to the first author and the Graduate Program of the Department of Physical Oceanography at CICESE for additional financial support to the first author and for access to the Tsunami cluster. The authors

thankfully acknowledge computer resources, technical advice and support provided by Laboratorio Nacional de Supercómputo del Sureste de México (LNS) through project No. 201803026. We also thank Christopher L. Castro, Ramón Fuentes Franco, and Julio Sheinbaum for their helpful comments when discussing the manuscript. J. Sheinbaum also provided access to the Kanik cluster. In addition, we thank three anonymous reviewers for their comments.

**Conflicts of Interest:** The authors declare no conflict of interest.

## References

1. Bluestein, H.B. *Synoptic-Dynamic Meteorology in Midlatitudes: Observations and Theory of Weather Systems*; Taylor & Francis: Abingdon, UK, 1992; Volume 2.
2. Holton, J. *An Introduction to Dynamic Meteorology*; International Geophysics Series; Academic Press: San Diego, CA, USA, 1992.
3. Serreze, M.C.; Francis, J.A. The Arctic Amplification debate. *Clim. Chang.* **2006**, *76*, 241–264. [[CrossRef](#)]
4. Screen, J.A.; Simmonds, I. The central role of diminishing sea ice in recent Arctic temperature amplification. *Nature* **2010**, *464*, 1334. [[CrossRef](#)] [[PubMed](#)]
5. Cohen, J.; Screen, J.A.; Furtado, J.C.; Barlow, M.; Whittleston, D.; Coumou, D.; Francis, J.; Dethloff, K.; Entekhabi, D.; Overland, J.; et al. Recent Arctic amplification and extreme mid-latitude weather. *Nat. Geosci.* **2014**, *7*, 627–637. [[CrossRef](#)]
6. IPCC. *Climate Change 2021—The Physical Science Basis. Contribution of Working Group I to the Sixth Assessment Report of the Intergovernmental Panel on Climate Change*; Cambridge University Press: Cambridge, UK, 2021.
7. Francis, J.A.; Vavrus, S.J. Evidence linking Arctic amplification to extreme weather in mid-latitudes. *Geophys. Res. Lett.* **2012**, *39*, 1–6. [[CrossRef](#)]
8. Yang, H.; Lohmann, G.; Lu, J.; Gowan, E.J.; Shi, X.; Liu, J.; Wang, Q. Tropical expansion driven by poleward advancing midlatitude meridional temperature gradients. *J. Geophys. Res. Atmos.* **2020**, *125*, e2020JD033158. [[CrossRef](#)]
9. Yang, H.; Lu, J.; Wang, Q.; Shi, X.; Lohmann, G. Decoding the dynamics of poleward shifting climate zones using aqua-planet model simulations. *Clim. Dyn.* **2022**, *58*, 3513–3526. [[CrossRef](#)]
10. Harvey, B.; Shaffrey, L.; Woollings, T. Equator-to-pole temperature differences and the extra-tropical storm track responses of the CMIP5 climate models. *Clim. Dyn.* **2014**, *43*, 1171–1182. [[CrossRef](#)]
11. Barnes, E.A.; Screen, J.A. The impact of Arctic warming on the midlatitude jet-stream: Can it? Has it? Will it? *Wiley Interdiscip. Rev. Clim. Chang.* **2015**, *6*, 277–286. [[CrossRef](#)]
12. Blackport, R.; Kushner, P.J. Isolating the atmospheric circulation response to Arctic sea ice loss in the coupled climate system. *J. Clim.* **2017**, *30*, 2163–2185. [[CrossRef](#)]
13. Vavrus, S.J. The influence of Arctic amplification on mid-latitude weather and climate. *Curr. Clim. Chang. Rep.* **2018**, *4*, 238–249. [[CrossRef](#)]
14. Strong, C.; Davis, R.E. Winter jet stream trends over the Northern Hemisphere. *Q. J. R. Meteorol. Soc. J. Atmos. Sci. Appl. Meteorol. Phys. Oceanogr.* **2007**, *133*, 2109–2115. [[CrossRef](#)]
15. Pena-Ortiz, C.; Gallego, D.; Ribera, P.; Ordonez, P.; Alvarez-Castro, M.D.C. Observed trends in the global jet stream characteristics during the second half of the 20th century. *J. Geophys. Res. Atmos.* **2013**, *118*, 2702–2713. [[CrossRef](#)]
16. Maher, P.; Kelleher, M.E.; Sansom, P.G.; Methven, J. Is the subtropical jet shifting poleward? *Clim. Dyn.* **2020**, *54*, 1741–1759. [[CrossRef](#)]
17. Manney, G.L.; Hegglin, M.I.; Lawrence, Z.D. Seasonal and regional signatures of ENSO in upper tropospheric jet characteristics from reanalyses. *J. Clim.* **2021**, *34*, 9181–9200. [[CrossRef](#)]
18. Archer, C.L.; Caldeira, K. Historical trends in the jet streams. *Geophys. Res. Lett.* **2008**, *35*. [[CrossRef](#)]
19. Thapa, U.K.; St. George, S.; Trouet, V. Poleward Excursions by the Himalayan Subtropical Jet Over the Past Four Centuries. *Geophys. Res. Lett.* **2020**, *47*, e2020GL089631. [[CrossRef](#)]
20. Francis, J.A.; Vavrus, S.J. Evidence for a wavier jet stream in response to rapid Arctic warming. *Environ. Res. Lett.* **2015**, *10*, 014005. [[CrossRef](#)]
21. Butler, A.H.; Thompson, D.W.; Heikes, R. The steady-state atmospheric circulation response to climate change-like thermal forcings in a simple general circulation model. *J. Clim.* **2010**, *23*, 3474–3496. [[CrossRef](#)]
22. Deser, C.; Tomas, R.; Alexander, M.; Lawrence, D.; Deser, C.; Tomas, R.; Alexander, M.; Lawrence, D. The Seasonal Atmospheric Response to Projected Arctic Sea Ice Loss in the Late Twenty-First Century. *J. Clim.* **2010**, *23*, 333–351. [[CrossRef](#)]
23. Screen, J.A. Influence of Arctic sea ice on European summer precipitation. *Environ. Res. Lett.* **2013**, *8*, 044015. [[CrossRef](#)]
24. Peings, Y.; Magnusdottir, G. Response of the Wintertime Northern Hemisphere Atmospheric Circulation to Current and Projected Arctic Sea Ice Decline: A Numerical Study with CAM5. *J. Clim.* **2014**, *27*, 244–264. [[CrossRef](#)]
25. Petrie, R.E.; Shaffrey, L.C.; Sutton, R.T. Atmospheric impact of Arctic sea ice loss in a coupled ocean–atmosphere simulation. *J. Clim.* **2015**, *28*, 9606–9622. [[CrossRef](#)]
26. Baker, H.S.; Woollings, T.; Mbengue, C. Eddy-driven jet sensitivity to diabatic heating in an idealized GCM. *J. Clim.* **2017**, *30*, 6413–6431. [[CrossRef](#)]
27. Zappa, G.; Pithan, F.; Shepherd, T.G. Multimodel evidence for an atmospheric circulation response to Arctic sea ice loss in the CMIP5 future projections. *Geophys. Res. Lett.* **2018**, *45*, 1011–1019. [[CrossRef](#)]

28. Smith, D.M.; Eade, R.; Andrews, M.; Ayres, H.; Clark, A.; Chripko, S.; Deser, C.; Dunstone, N.; García-Serrano, J.; Gastineau, G.; et al. Robust but weak winter atmospheric circulation response to future Arctic sea ice loss. *Nat. Commun.* **2022**, *13*, 1–15. [[CrossRef](#)]
29. Barnes, E.A.; Simpson, I.R. Seasonal sensitivity of the Northern Hemisphere jet streams to Arctic temperatures on subseasonal time scales. *J. Clim.* **2017**, *30*, 10117–10137. [[CrossRef](#)]
30. McKenna, C.M.; Bracegirdle, T.J.; Shuckburgh, E.F.; Haynes, P.H.; Joshi, M.M. Arctic sea ice loss in different regions leads to contrasting Northern Hemisphere impacts. *Geophys. Res. Lett.* **2018**, *45*, 945–954. [[CrossRef](#)]
31. Barnes, E.A. Revisiting the evidence linking Arctic amplification to extreme weather in midlatitudes. *Geophys. Res. Lett.* **2013**, *40*, 4734–4739. [[CrossRef](#)]
32. Screen, J.A.; Simmonds, I. Exploring links between Arctic amplification and mid-latitude weather. *Geophys. Res. Lett.* **2013**, *40*, 959–964. [[CrossRef](#)]
33. Blackport, R.; Screen, J.A. Insignificant effect of Arctic amplification on the amplitude of midlatitude atmospheric waves. *Sci. Adv.* **2020**, *6*, 1–10. [[CrossRef](#)]
34. Hall, R.; Erdélyi, R.; Hanna, E.; Jones, J.M.; Scaife, A.A. Drivers of North Atlantic polar front jet stream variability. *Int. J. Climatol.* **2015**, *35*, 1697–1720. [[CrossRef](#)]
35. Chen, G.; Lu, J.; Frierson, D.M. Phase speed spectra and the latitude of surface westerlies: Interannual variability and global warming trend. *J. Clim.* **2008**, *21*, 5942–5959. [[CrossRef](#)]
36. Lu, J.; Chen, G.; Frierson, D.M. Response of the zonal mean atmospheric circulation to El Niño versus global warming. *J. Clim.* **2008**, *21*, 5835–5851. [[CrossRef](#)]
37. Staten, P.W.; Lu, J.; Grise, K.M.; Davis, S.M.; Birner, T. Re-examining tropical expansion. *Nat. Clim. Chang.* **2018**, *8*, 768–775. [[CrossRef](#)]
38. Allen, R.J.; Norris, J.R.; Kovilakam, M. Influence of anthropogenic aerosols and the Pacific Decadal Oscillation on tropical belt width. *Nat. Geosci.* **2014**, *7*, 270–274. [[CrossRef](#)]
39. Mantsis, D.F.; Sherwood, S.; Allen, R.; Shi, L. Natural variations of tropical width and recent trends. *Geophys. Res. Lett.* **2017**, *44*, 3825–3832. [[CrossRef](#)]
40. Woollings, T.; Hannachi, A.; Hoskins, B. Variability of the North Atlantic eddy-driven jet stream. *Q. J. R. Meteorol. Soc.* **2010**, *136*, 856–868. [[CrossRef](#)]
41. Woollings, T.; Czuchnicki, C.; Franzke, C. Twentieth century North Atlantic jet variability. *Q. J. R. Meteorol. Soc.* **2014**, *140*, 783–791. [[CrossRef](#)]
42. Thompson, D.W.; Wallace, J.M. The Arctic Oscillation signature in the wintertime geopotential height and temperature fields. *Geophys. Res. Lett.* **1998**, *25*, 1297–1300. [[CrossRef](#)]
43. Thompson, D.W.; Wallace, J.M. Annular modes in the extratropical circulation. Part I: Month-to-month variability. *J. Clim.* **2000**, *13*, 1000–1016. [[CrossRef](#)]
44. Ambaum, M.H.; Hoskins, B.J.; Stephenson, D.B. Arctic oscillation or North Atlantic oscillation? *J. Clim.* **2001**, *14*, 3495–3507. [[CrossRef](#)]
45. Barnston, A.G.; Livezey, R.E. Classification, seasonality and persistence of low-frequency atmospheric circulation patterns. *Mon. Weather Rev.* **1987**, *115*, 1083–1126. [[CrossRef](#)]
46. Hurrell, J.W.; Holland, M.M.; Gent, P.R.; Ghan, S.; Kay, J.E.; Kushner, P.J.; Lamarque, J.F.; Large, W.G.; Lawrence, D.; Lindsay, K.; et al. The community earth system model: A framework for collaborative research. *Bull. Am. Meteorol. Soc.* **2013**, *94*, 1339–1360. [[CrossRef](#)]
47. Conley, A.J.; Garcia, R.; Kinnison, D.; Lamarque, J.F.; Marsh, D.; Mills, M.; Smith, A.K.; Tilmes, S.; Vitt, F.; Morrison, H.; et al. Description of the NCAR community atmosphere model (CAM 5.0). *NCAR Tech. Note* **2012**, *3*. Available online: <https://www.cesm.ucar.edu/models/cesm1.0/cam/> (accessed on 25 January 2022).
48. Lawrence, D.M.; Oleson, K.W.; Flanner, M.G.; Thornton, P.E.; Swenson, S.C.; Lawrence, P.J.; Zeng, X.; Yang, Z.L.; Levis, S.; Sakaguchi, K.; et al. Parameterization improvements and functional and structural advances in version 4 of the Community Land Model. *J. Adv. Model. Earth Syst.* **2011**, *3*. [[CrossRef](#)]
49. Gates, W.; Boyle, J.; Covey, C.; Dease, C.; Doutriaux, C.; Drach, R.; Fiorino, M.; Gleckler, P.; Hnilo, J.; Marlais, S.M.; et al. An Overview of the Results of the Atmospheric Model Intercomparison Project (AMIP I). *Bull. Am. Meteorol. Soc.* **1999**, *80*, 29–55. [[CrossRef](#)]
50. Rayner, N.A. Global analyses of sea surface temperature, sea ice, and night marine air temperature since the late nineteenth century. *J. Geophys. Res.* **2003**, *108*, 4407. [[CrossRef](#)]
51. Lamarque, J.F.; Bond, T.C.; Eyring, V.; Granier, C.; Heil, A.; Klimont, Z.; Lee, D.; Liousse, C.; Mieville, A.; Owen, B.; et al. Historical (1850–2000) gridded anthropogenic and biomass burning emissions of reactive gases and aerosols: Methodology and application. *Atmos. Chem. Phys.* **2010**, *10*, 7017–7039. [[CrossRef](#)]
52. Kay, J.E.; Deser, C.; Phillips, A.; Mai, A.; Hannay, C.; Strand, G.; Arblaster, J.M.; Bates, S.C.; Danabasoglu, G.; Edwards, J.; et al. The community earth system model (CESM) large ensemble project: A community resource for studying climate change in the presence of internal climate variability. *Bull. Am. Meteorol. Soc.* **2015**, *96*, 1333–1349. [[CrossRef](#)]
53. Deser, C.; Phillips, A.; Bourdette, V.; Teng, H. Uncertainty in climate change projections: The role of internal variability. *Clim. Dyn.* **2012**, *38*, 527–546. [[CrossRef](#)]

54. Neelin, J.D.; Battisti, D.S.; Hirst, A.C.; Jin, F.F.; Wakata, Y.; Yamagata, T.; Zebiak, S.E. ENSO theory. *J. Geophys. Res. Ocean* **1998**, *103*, 14261–14290. [[CrossRef](#)]
55. Wallace, J.; Rasmusson, E.; Mitchell, T.; Kousky, V.; Sarachik, E.; Von Storch, H. On the structure and evolution of ENSO-related climate variability in the tropical Pacific: Lessons from TOGA. *J. Geophys. Res. Ocean* **1998**, *103*, 14241–14259. [[CrossRef](#)]
56. Timmermann, A.; An, S.I.; Kug, J.S.; Jin, F.F.; Cai, W.; Capotondi, A.; Cobb, K.M.; Lengaigne, M.; McPhaden, M.J.; Stuecker, M.F.; et al. El Niño–southern oscillation complexity. *Nature* **2018**, *559*, 535–545. [[CrossRef](#)]
57. Kalnay, E.; Kanamitsu, M.; Kistler, R.; Collins, W.; Deaven, D.; Gandin, L.; Iredell, M.; Saha, S.; White, G.; Woollen, J.; et al. The NCEP/NCAR reanalysis 40-year project. *Bull. Am. Meteorol. Soc* **1996**, *77*, 437–471. [[CrossRef](#)]
58. Li, C.; Wettstein, J.J. Thermally driven and eddy-driven jet variability in reanalysis. *J. Clim.* **2012**, *25*, 1587–1596. [[CrossRef](#)]
59. Hamming, R.W. *Digital Filters*, 3rd ed.; Courier Corporation: Englewood Cliffs, NJ, USA, 1998.
60. Wallace, J.M.; Lim, G.H.; Blackmon, M.L. Relationship between cyclone tracks, anticyclone tracks and baroclinic waveguides. *J. Atmos. Sci.* **1988**, *45*, 439–462. [[CrossRef](#)]
61. Afargan, H.; Kaspi, Y. A midwinter minimum in North Atlantic storm track intensity in years of a strong jet. *Geophys. Res. Lett.* **2017**, *44*, 12–511. [[CrossRef](#)]
62. Yuval, J.; Afargan, H.; Kaspi, Y. The relation between the seasonal changes in jet characteristics and the Pacific midwinter minimum in eddy activity. *Geophys. Res. Lett.* **2018**, *45*, 9995–10002. [[CrossRef](#)]
63. Afargan-Gerstman, H.; Domeisen, D.I. Pacific modulation of the North Atlantic storm track response to sudden stratospheric warming events. *Geophys. Res. Lett.* **2020**, *47*, e2019GL085007. [[CrossRef](#)]
64. Sen, P.K. Estimates of the regression coefficient based on Kendall’s tau. *J. Am. Stat. Assoc.* **1968**, *63*, 1379–1389. [[CrossRef](#)]
65. Kendall, M. *Rank Correlation Methods*; Charles Griffin: London, UK, 1975.
66. Wallace, J.M.; Gutzler, D.S. Teleconnections in the geopotential height field during the Northern Hemisphere winter. *Mon. Weather Rev.* **1981**, *109*, 784–812. [[CrossRef](#)]
67. Overland, J.E.; Wood, K.R.; Wang, M. Warm Arctic—Cold continents: climate impacts of the newly open Arctic Sea. *Polar Res.* **2011**, *30*, 15787. [[CrossRef](#)]
68. Mori, M.; Watanabe, M.; Shiogama, H.; Inoue, J.; Kimoto, M. Robust Arctic sea-ice influence on the frequent Eurasian cold winters in past decades. *Nat. Geosci.* **2014**, *7*, 869–873. [[CrossRef](#)]
69. Kug, J.S.; Jeong, J.H.; Jang, Y.S.; Kim, B.M.; Folland, C.K.; Min, S.K.; Son, S.W. Two distinct influences of Arctic warming on cold winters over North America and East Asia. *Nat. Geosci.* **2015**, *8*, 759–762. [[CrossRef](#)]
70. Chen, L.; Francis, J.; Hanna, E. The “Warm-Arctic/Cold-continents” pattern during 1901–2010. *Int. J. Climatol.* **2018**, *38*, 5245–5254. [[CrossRef](#)]
71. Honda, M.; Inoue, J.; Yamane, S. Influence of low Arctic sea-ice minima on anomalously cold Eurasian winters. *Geophys. Res. Lett.* **2009**, *36*. [[CrossRef](#)]
72. Nakamura, T.; Yamazaki, K.; Iwamoto, K.; Honda, M.; Miyoshi, Y.; Ogawa, Y.; Ukita, J. A negative phase shift of the winter AO/NAO due to the recent Arctic sea-ice reduction in late autumn. *J. Geophys. Res. Atmos.* **2015**, *120*, 3209–3227. [[CrossRef](#)]
73. Wu, A.; Hsieh, W.W.; Boer, G.J.; Zwiers, F.W. Changes in the Arctic Oscillation under increased atmospheric greenhouse gases. *Geophys. Res. Lett.* **2007**, *34*. [[CrossRef](#)]
74. Deser, C.; Sun, L.; Tomas, R.A.; Screen, J. Does ocean coupling matter for the northern extratropical response to projected Arctic sea ice loss? *Geophys. Res. Lett.* **2016**, *43*, 2149–2157. [[CrossRef](#)]
75. Tomas, R.A.; Deser, C.; Sun, L. The role of ocean heat transport in the global climate response to projected Arctic sea ice loss. *J. Clim.* **2016**, *29*, 6841–6859. [[CrossRef](#)]
76. Screen, J.A.; Deser, C.; Smith, D.M.; Zhang, X.; Blackport, R.; Kushner, P.J.; Oudar, T.; McCusker, K.E.; Sun, L. Consistency and discrepancy in the atmospheric response to Arctic sea-ice loss across climate models. *Nat. Geosci.* **2018**, *11*, 155–163. [[CrossRef](#)]
77. McCusker, K.E.; Kushner, P.J.; Fyfe, J.C.; Sigmond, M.; Kharin, V.V.; Bitz, C.M. Remarkable separability of circulation response to Arctic sea ice loss and greenhouse gas forcing. *Geophys. Res. Lett.* **2017**, *44*, 7955–7964. [[CrossRef](#)]
78. Oudar, T.; Sanchez-Gomez, E.; Chauvin, F.; Cattiaux, J.; Terray, L.; Cassou, C. Respective roles of direct GHG radiative forcing and induced Arctic sea ice loss on the Northern Hemisphere atmospheric circulation. *Clim. Dyn.* **2017**, *49*, 3693–3713. [[CrossRef](#)]
79. Kim, B.M.; Son, S.W.; Min, S.K.; Jeong, J.H.; Kim, S.J.; Zhang, X.; Shim, T.; Yoon, J.H. Weakening of the stratospheric polar vortex by Arctic sea-ice loss. *Nat. Commun.* **2014**, *5*. [[CrossRef](#)]
80. Sun, L.; Deser, C.; Tomas, R.A. Mechanisms of stratospheric and tropospheric circulation response to projected Arctic sea ice loss. *J. Clim.* **2015**, *28*, 7824–7845. [[CrossRef](#)]
81. Wu, Y.; Smith, K.L. Response of Northern Hemisphere midlatitude circulation to Arctic amplification in a simple atmospheric general circulation model. *J. Clim.* **2016**, *29*, 2041–2058. [[CrossRef](#)]
82. Bao, M.; Wallace, J.M. Cluster analysis of Northern Hemisphere wintertime 500-hPa flow regimes during 1920–2014. *J. Atmos. Sci.* **2015**, *72*, 3597–3608. [[CrossRef](#)]
83. Kim, S.H.; Ha, K.J. Two leading modes of Northern Hemisphere blocking variability in the boreal wintertime and their relationship with teleconnection patterns. *Clim. Dyn.* **2015**, *44*, 2479–2491. [[CrossRef](#)]
84. Messori, G.; Caballero, R.; Gaetani, M. On cold spells in North America and storminess in western Europe. *Geophys. Res. Lett.* **2016**, *43*, 6620–6628. [[CrossRef](#)]

85. Park, H.J.; Ahn, J.B. Combined effect of the Arctic Oscillation and the Western Pacific pattern on East Asia winter temperature. *Clim. Dyn.* **2016**, *46*, 3205–3221. [[CrossRef](#)]
86. Woollings, T.; Hannachi, A.; Hoskins, B.; Turner, A. A regime view of the North Atlantic Oscillation and its response to anthropogenic forcing. *J. Clim.* **2010**, *23*, 1291–1307. [[CrossRef](#)]
87. Seierstad, I.A.; Bader, J. Impact of a projected future Arctic Sea Ice reduction on extratropical storminess and the NAO. *Clim. Dyn.* **2009**, *33*, 937–943. [[CrossRef](#)]
88. Blackport, R.; Screen, J.A. Observed statistical connections overestimate the causal effects of arctic sea ice changes on midlatitude winter climate. *J. Clim.* **2021**, *34*, 3021–3038. [[CrossRef](#)]
89. Hallam, S.; Josey, S.A.; McCarthy, G.D.; Hirschi, J.J.M. A regional (land–ocean) comparison of the seasonal to decadal variability of the Northern Hemisphere jet stream 1871–2011. *Clim. Dyn.* **2022**, 1–22. doi: 10.1007/s00382-022-06185-5. [[CrossRef](#)]
90. Thompson, D.W.; Solomon, S.; Kushner, P.J.; England, M.H.; Grise, K.M.; Karoly, D.J. Signatures of the Antarctic ozone hole in Southern Hemisphere surface climate change. *Nat. Geosci.* **2011**, *4*, 741–749. [[CrossRef](#)]
91. Orr, A.; Bracegirdle, T.J.; Hosking, J.S.; Feng, W.; Roscoe, H.K.; Haigh, J.D. Strong dynamical modulation of the cooling of the polar stratosphere associated with the Antarctic ozone hole. *J. Clim.* **2012**, *26*, 662–668. [[CrossRef](#)]
92. Wu, Q.; Zhang, X. Observed forcing–feedback processes between Northern Hemisphere atmospheric circulation and Arctic sea ice coverage. *J. Geophys. Res. Atmos.* **2010**, *115*, doi: 10.1029/2009JD013574. [[CrossRef](#)]
93. Zhang, W.; Li, J.; Zhao, X. Sea surface temperature cooling mode in the Pacific cold tongue. *J. Geophys. Res. Ocean.* **2010**, *115*. [[CrossRef](#)]
94. Grassi, B.; Redaelli, G.; Canziani, P.O.; Visconti, G. Effects of the PDO phase on the tropical belt width. *J. Clim.* **2012**, *25*, 3282–3290. [[CrossRef](#)]
95. Kosaka, Y.; Xie, S.P. Recent global-warming hiatus tied to equatorial Pacific surface cooling. *Nature* **2013**, *501*, 403–407. [[CrossRef](#)]
96. McGregor, S.; Timmermann, A.; Stuecker, M.F.; England, M.H.; Merrifield, M.; Jin, F.F.; Chikamoto, Y. Recent Walker circulation strengthening and Pacific cooling amplified by Atlantic warming. *Nat. Clim. Chang.* **2014**, *4*, 888–892. [[CrossRef](#)]
97. Grise, K.M.; Davis, S.M.; Simpson, I.R.; Waugh, D.W.; Fu, Q.; Allen, R.J.; Rosenlof, K.H.; Ummenhofer, C.C.; Karauskas, K.B.; Maycock, A.C.; et al. Recent tropical expansion: Natural variability or forced response? *J. Clim.* **2019**, *32*, 1551–1571. [[CrossRef](#)]
98. Henley, B.J.; Gergis, J.; Karoly, D.J.; Power, S.; Kennedy, J.; Folland, C.K. A tripole index for the interdecadal Pacific oscillation. *Clim. Dyn.* **2015**, *45*, 3077–3090. [[CrossRef](#)]
99. Newman, M.; Alexander, M.A.; Ault, T.R.; Cobb, K.M.; Deser, C.; Di Lorenzo, E.; Mantua, N.J.; Miller, A.J.; Minobe, S.; Nakamura, H.; et al. The Pacific decadal oscillation, revisited. *J. Clim.* **2016**, *29*, 4399–4427. [[CrossRef](#)]
100. Feng, X.; Ding, Q.; Wu, L.; Jones, C.; Baxter, I.; Tardif, R.; Stevenson, S.; Emile-Geay, J.; Mitchell, J.; Carvalho, L.M.; et al. A Multidecadal-Scale Tropically Driven Global Teleconnection over the Past Millennium and Its Recent Strengthening. *J. Clim.* **2021**, *34*, 2549–2565. [[CrossRef](#)]
101. Sun, X.; Ding, Q.; Wang, S.Y.; Topal, D.; Castro, C.; Teng, H.; Luo, R.; Ding, Y. Enhanced jet stream waviness induced by suppressed tropical Pacific convection during boreal summer. *Nat. Commun.* **2022**, *13*, 1–10. [[CrossRef](#)]
102. Strong, C.; Davis, R.E. Variability in the position and strength of winter jet stream cores related to Northern Hemisphere teleconnections. *J. Clim.* **2008**, *21*, 584–592. [[CrossRef](#)]
103. Barton, N.P.; Ellis, A.W. Variability in wintertime position and strength of the North Pacific jet stream as represented by re-analysis data. *Int. J. Climatol. J. R. Meteorol. Soc.* **2009**, *29*, 851–862. [[CrossRef](#)]
104. Athanasiadis, P.J.; Wallace, J.M.; Wettstein, J.J. Patterns of wintertime jet stream variability and their relation to the storm tracks. *J. Atmos. Sci.* **2010**, *67*, 1361–1381. [[CrossRef](#)]
105. Liu, X.; Grise, K.M.; Schmidt, D.F.; Davis, R.E. Regional characteristics of variability in the Northern Hemisphere wintertime polar front jet and subtropical jet in observations and CMIP6 models. *J. Geophys. Res. Atmos.* **2021**, *126*, e2021JD034876. [[CrossRef](#)]
106. Cassano, E.N.; Cassano, J.J.; Higgins, M.E.; Serreze, M.C. Atmospheric impacts of an Arctic sea ice minimum as seen in the Community Atmosphere Model. *Int. J. Climatol.* **2014**, *34*, 766–779. [[CrossRef](#)]